Seventh International Conference on Computational Fluid Dynamics (ICCFD7), Big Island, Hawaii, July 9-13, 2012

ICCFD7-3304

Three-dimensional thin film flow over topography: full Navier-Stokes solutions

S. Veremieiev*, H.M. Thompson* and P.H. Gaskell*
Corresponding author: s.veremieiev@leeds.ac.uk

* School of Mechanical Engineering, University of Leeds, Leeds, LS2 9JT, UK.

Abstract: The problem of gravity-driven film flow over trench topography is investigated via novel solutions of the governing three-dimensional Navier-Stokes system of equations based on a finite element formulation, with the free surface parametrisation employing the method of spines. The resulting numerical analogue is solved using a parallel multifrontal method together with a memory-efficient out-of-core storage approach. Adopting this methodology allows simultaneous exploration of the internal flow structure/topology and the associated free-surface disturbance generated in terms of the geometry of the trench and the presence of inertia. Comparisons are drawn with the corresponding free-surface disturbances predicted using a model based on the long-wave approximation.

Keywords: Thin Liquid Films, Free Surface Flow, Finite Elements, Flow Topology.

1 Introduction

The deposition of thin, liquid films onto naturally-occurring and functional surfaces is ubiquitous throughout engineering, scientific and technological applications; see e.g. the recent review by [1]. Examples from nature include the control of disease in plants, [2], and the redistribution of the liquid linings of respiratory systems [3]. These flows also form an important component of several industrial applications, including the coating of papers and plastics in the inkjet and photographic industries, [4], direct-write printing of electronic circuits, [5], and the manufacture of anti-reflective coatings, [6].

The focus of this paper is that of obtaining detailed finite element solutions of the full Navier-Stokes (N-S) equations for three-dimensional film flow over a rectangular trench topography revealing (i) the internal flow structure/topology and (ii) the free-surface disturbance generated; the latter are compared to the same obtained using a model based on the so-called depth-averaged form (DAF), [7], consistent with the well-known long-wave approximation. Previous numerical studies reporting related finite element solutions of the N-S equations have been confined to film flow over two-dimensional, spanwise, trench topographies only, see [8]. Note too, that Stokes solutions for three-dimensional film flow over a hemispheric obstacle and around a cylindrical occlusion have been reported recently; these were obtained using a boundary element approach, [9].

The flow problem of interest is formulated in Section 2, while Section 3 outlines the numerical methodology adopted. Results are presented in Section 4 for the internal flow structure/topology together with the corresponding free-surface disturbance experienced. Conclusions are drawn in Section 5.

2 Problem Formulation

Consider, as illustrated in Figure 1, the case of steady-state gravity-driven thin film flow down a planar surface containing a trench topography of depth S_0, length L_T and spanwise width W_T, that is inclined at an angle $\theta(\neq 0)$ to the horizontal. The liquid is assumed to be incompressible and to have constant density, ρ, dynamic viscosity, μ, and surface tension, σ. The chosen Cartesian streamwise, X, spanwise, Y, and

normal, Z, components of the coordinate vector, $\boldsymbol{X} = X\boldsymbol{i} + Y\boldsymbol{j} + Z\boldsymbol{k}$, are as indicated; $\boldsymbol{i}$, $\boldsymbol{j}$, $\boldsymbol{k}$ are the corresponding basis vectors of the coordinate system. The solution domain is bounded from below by the surface containing the trench, $Z = S(X,Y)$, from above by the free surface, $Z = F(X,Y)$, upstream and downstream by the inflow, $X = 0$, and outflow, $X = L_P$, planes, respectively, and to the left and right by the side planes at $Y = 0$ and $Y = W_P$. The resulting laminar flow is described by the Navier-Stokes and continuity equations (referred to subsequently as the N-S system of equations), namely:

$$\rho \boldsymbol{U} \cdot \nabla \boldsymbol{U} = -\nabla P + \nabla \cdot \boldsymbol{T} + \rho \boldsymbol{G}, \tag{1}$$

$$\nabla \cdot \boldsymbol{U} = 0, \tag{2}$$

where $\boldsymbol{U} = U\boldsymbol{i} + V\boldsymbol{j} + W\boldsymbol{k}$ and P are the fluid velocity and pressure, respectively; $\boldsymbol{T} = \mu\left(\nabla \boldsymbol{U} + (\nabla \boldsymbol{U})^T\right)$ is the viscous stress tensor, $\boldsymbol{G} = G_0\left(\boldsymbol{i}\sin\theta - \boldsymbol{k}\cos\theta\right)$ is the acceleration due to gravity where G_0 is the standard gravity constant.

Taking the reference length scale in all directions to be the asymptotic, or fully developed, film thickness, H_0, and scaling the velocities by the free-surface (maximum) velocity apropos the classic Nusselt solution, $U_0 = \rho G_0 H_0^2 \sin\theta / 2\mu$ and the pressure (stress tensor) by $P_0 = \mu U_0 / H_0$, equations (1) - (2) can be rewritten in non-dimensional form as:

$$\mathrm{Re}\boldsymbol{u} \cdot \nabla \boldsymbol{u} = -\nabla p + \nabla \cdot \boldsymbol{\tau} + \mathrm{St}\boldsymbol{g}, \tag{3}$$

$$\nabla \cdot \boldsymbol{u} = \boldsymbol{0}, \tag{4}$$

where $\boldsymbol{x} = x\boldsymbol{i} + y\boldsymbol{j} + z\boldsymbol{k}$, $\boldsymbol{u} = u\boldsymbol{i} + v\boldsymbol{j} + w\boldsymbol{k}$, p, $\boldsymbol{\tau}$ and $\boldsymbol{g} = \boldsymbol{G}/G_0$ are the non-dimensional coordinate, velocity, pressure, viscous stress tensor and gravity component, respectively. $\mathrm{Re} = \rho U_0 H_0 / \mu$ is the Reynolds number, $\mathrm{Ca} = \mu U_0 / \sigma$ is the capillary number and $\mathrm{St} = \rho G_0 H_0^2 / \mu U_0 = 2/\sin\theta$ the Stokes number.

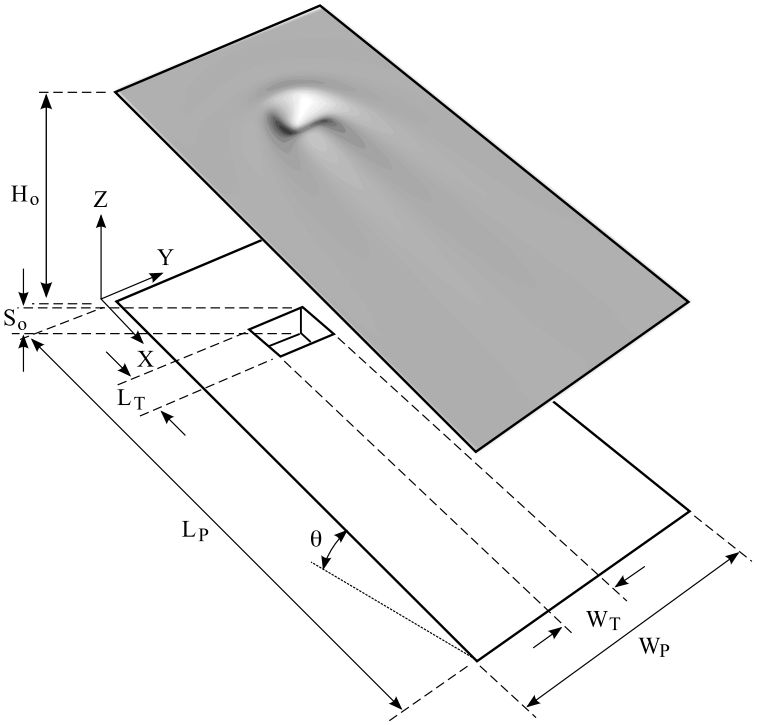

Figure 1: Schematic diagram of gravity-driven film flow over a well-defined trench topography, showing the coordinate system adopted and surface geometry.

The general problem definition is complete following the specification of appropriate no-slip, inflow/outflow, kinematic and free-surface normal and tangential stress boundary conditions:

$$\boldsymbol{u}|_{z=s} = 0, \tag{5}$$

$$h|_{x=0} = 1, \quad \boldsymbol{u}|_{x=0,l_p;y=0,w_p} = z\,(2-z)\,\boldsymbol{i}, \tag{6}$$

$$(\boldsymbol{n}\cdot\boldsymbol{u})\,|_{z=f} = 0, \tag{7}$$

$$-p|_{z=f} + (\boldsymbol{\tau}|_{z=f}\cdot\boldsymbol{n})\cdot\boldsymbol{n} = \frac{\kappa}{\mathrm{Ca}}, \tag{8}$$

$$(\boldsymbol{\tau}|_{z=f}\cdot\boldsymbol{n})\cdot\boldsymbol{t} = 0, \tag{9}$$

where h, s, f together with s_0, l_t, w_t, l_p and w_p correspond to their dimensional counterparts, $\boldsymbol{n} = \left(-\frac{\partial f}{\partial x}\boldsymbol{i} - \frac{\partial f}{\partial y}\boldsymbol{j} + \boldsymbol{k}\right)\cdot\left[\left(\frac{\partial f}{\partial x}\right)^2 + \left(\frac{\partial f}{\partial y}\right)^2 + 1\right]^{-1/2}$ is the unit normal vector pointing outward from the free surface, $\boldsymbol{t} = \left[\alpha_t\boldsymbol{i} + \beta_t\boldsymbol{j} + \left(\alpha_t\frac{\partial f}{\partial x} + \beta_t\frac{\partial f}{\partial y}\right)\boldsymbol{k}\right]\cdot\left[\alpha_t^2 + \beta_t^2 + \left(\alpha_t\frac{\partial f}{\partial x} + \beta_t\frac{\partial f}{\partial y}\right)^2\right]^{-1/2}$ is the unit vector tangential to the free surface and $\kappa = -\nabla\cdot\boldsymbol{n}$ is twice the mean curvature of the free surface that is taken to be positive when the surface is concave upwards. α_t and β_t are variables that define the direction of the tangent vector at any point in the tangent plane; thus equation (9) actually implies two boundary conditions. For convenience the coordinate system placed at the centre of the topography, (x_t, y_t), is denoted as: $(x^*, y^*) = (x - x_t, y - y_t)$. The spanwise symmetry of the topography is exploited enabling the governing N-S equations to be solved over half of the solution domain only by imposing the following boundary conditions at the symmetry plane:

$$\frac{\partial u}{\partial y}|_{y^*=0} = v|_{y^*=0} = \frac{\partial w}{\partial y}|_{y^*=0} = \frac{\partial p}{\partial y}|_{y^*=0} = \frac{\partial h}{\partial y}|_{y^*=0} = 0. \tag{10}$$

3 Method of Solution

The full N-S system of equations, (3) and (4), subject to the boundary conditions, (5) to (10), is solved using an appropriate finite element formulation, a complicating feature being the presence of a bounding free-surface, whose shape and position are not known a priori. In line with the underpinnings of the finite element method, the unknown velocity, pressure and grid coordinate fields are expanded in terms of basis functions:

$$\boldsymbol{u} = \sum_{i=1}^{n^i}\boldsymbol{u}_i\phi_i, \quad p = \sum_{j=1}^{n^j}p_j\psi_j, \quad \boldsymbol{x} = \sum_{i=1}^{n^i}\boldsymbol{x}_i\phi_i, \tag{11}$$

where $i \in \left[1, n^i\right]$, $j \in \left[1, n^j\right]$, $\boldsymbol{u}_i = u_i\boldsymbol{i} + v_i\boldsymbol{j} + w_i\boldsymbol{k}$, p_j and $\boldsymbol{x}_i = x_i\boldsymbol{i} + y_i\boldsymbol{j} + z_i\boldsymbol{k}$ are the unknown nodal values of the velocity, pressure and coordinate fields, respectively; n^i is the total number of $\boldsymbol{u}/\boldsymbol{x}$-nodes and n^j is the total number of p-nodes; ϕ_i are basis functions for $\boldsymbol{u}/\boldsymbol{x}$ and ψ_j are basis functions for p. V10/P4/X10 (10 $\boldsymbol{u}/\boldsymbol{x}$-nodes and 4 p-nodes) tetrahedral elements are used with a 'mixed-interpolation' formulation employing linear basis functions for pressure and quadratic basis functions for velocities and mesh coordinates, [10], satisfying the so called LBB stability condition.

A popular Bubnov-Galerkin weighted residual formulation is employed for the discretisation of equations (3), (4) and (7) over the problem domain, Ω, and the free-surface:

$$\int_\Omega\Big[\left(-\mathrm{Re}\boldsymbol{u}\otimes\boldsymbol{u} - p\boldsymbol{I} + \boldsymbol{\tau}\right)\nabla\phi_i - \mathrm{St}\boldsymbol{g}\phi_i\Big]d\Omega + \frac{1}{\mathrm{Ca}}\int_f\Big[\nabla\phi_i - \boldsymbol{n}\left(\boldsymbol{n}\cdot\nabla\phi_i\right)\Big]df = \boldsymbol{0}, \tag{12}$$

$$\int_\Omega\nabla\cdot\boldsymbol{u}\psi_j d\Omega = 0, \tag{13}$$

$$\int_f(\boldsymbol{n}\cdot\boldsymbol{u})\,\phi_k df = 0, \tag{14}$$

where $\boldsymbol{I}$ is the unity tensor, $\otimes$ denotes dyadic product of two vectors and $k \in \left[1, n^k\right]$ $\left(n^k < n^i\right)$ are the free-surface $\boldsymbol{u}/\boldsymbol{x}$-nodes; application of the divergence theorem has lowered the order of spatial derivatives and the remaining boundary conditions (5) - (10) have been incorporated. The spine method, [11], is used to relate the positions of the Lagrangian mesh nodes, $\boldsymbol{x}_i$, to a set of free-surface parameters called spinal distances,

h_k, whose values determine how the mesh changes in response to the moving free-surface boundary:

$$\boldsymbol{x}_i = \boldsymbol{x}_i^b + \Delta_{i,k} h_k \boldsymbol{d}_i, \tag{15}$$

where $\boldsymbol{x}_i^b$ and $\boldsymbol{d}_i$ are the fixed base nodes and fixed direction vectors of the spines, while $\Delta_{i,k}$ is Boolean matrix, whose elements are 1, if the global node i lies on the spine k, and 0, otherwise.

The integrals (12) to (14) are calculated numerically using symmetric Gaussian quadrature. The no-slip and inflow/outflow boundary conditions, (5) and (6), are imposed by replacing the corresponding weighted residual momentum or kinematic boundary equations with the desired velocity or spine value there. The Nusselt velocity and pressure profiles are chosen as initial approximations for the velocity and pressure fields, respectively; the initial approximation for the spine heights is taken to be the one corresponding to a flat free-surface profile. For two-dimensional flow, streamlines are found by contouring the streamfunction, in three-dimensions fluid flow trajectories are obtained by integrating along path lines using the Matlab 7.9 *streamline* function.

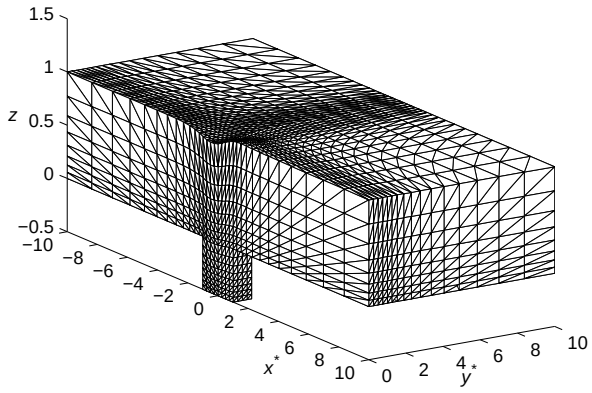

Figure 2: A typical irregular finite element grid comprised of tetrahedral elements for three-dimensional thin film flow over a localised trench topography with $l_t = w_t = 2$ and $s_0 = 0.5$. For illustration purposes the number of elements in the half solution domain is set to $6 \times 32 \times 16 \times 8$ and $6 \times 8 \times 4 \times 10$ outwith and over the trench, respectively.

Accurate and fast solutions to large three-dimensional free-surface problems can only be achieved via a parallel computing strategy. Thus the system of discrete equations (12) - (14) is linearised by the Newton-Raphson method with the Jacobians evaluated analytically and solved using a parallel multifrontal method, that is a variant of Gaussian elimination initially developed for indefinite sparse symmetric linear systems by [12] and then extended to unsymmetric matrices, [13]. A widely used and efficient parallel implementation of the method from the MUltifrontal Massively Parallel sparse direct Solver (MUMPS) is employed, which is written in Fortran 90 with a C interface and invokes the well-known memory distributed parallel message passing interface (MPI) protocol, see [14].

Solution via the multifrontal method is comprised of three steps. The first is the analysis step involving the partitioning of the computational domain and computation of an efficient assembly tree; here the analysis stage is performed using an efficient multilevel nested dissection algorithm provided within a parallel routine of the ParMETIS implementation, see [15]. The second step is the factorisation step and proceeds by performing a succession of partial factorisations of small dense matrices called 'frontal matrices', that are associated with each node of the assembly tree, see [12, 13] for more detail. The final, third step is the solution step based on performing forward elimination and backward substitution for the factors obtained and the right-hand-side.

The multifrontal method requires a large amount of memory, that can be much larger than the physical (in-core) memory available on the system thus out-of-core memory is required as well, see [16]. This approach assumes that only the frontal matrices are held in main memory while the factors, which are accessed only during the final solution step, can be held in direct-access files stored on the hard drive; it allows much larger problems to be considered and reduces memory usage significantly (by a factor 5 to 10 on 1 to 4 processors,

and a factor around 2 on 16 to 128 processors). In addition in a parallel context, increasing the number of processors, and therefore available physical memory, can help keep large frontal matrices in-core.

Typically 2 or 3 Newton-Raphson iterations are required to reduce the norm of the residuals to below 10^{-6} with the Jacobians calculated analytically. The number of elements in the mesh was systematically increased until the maximum change in the predicted free-surface profiles on consecutive meshes became less than 0.05%. As a result an irregular finite element grid arrangement was employed with elements mainly concentrated near to but especially inside the topography in order to capture the associated eddy structure present, see Figure 2.

4 Results

The associated hydrodynamic stability limit for a gravity-driven thin film flowing down a flat inclined substrate, [17] and [18], is adhered to by taking a substrate inclination angle of $\theta = 7^\circ$ requiring the Reynolds number to be less than $\mathrm{Re}_{crit} = \frac{5}{4}\cot\theta \approx 10.2$ for the free-surface flow to be considered strictly stable. A rectangular trench topography with $l_t = 2$, $s_0 = 1$, $l_p = w_p = 550$, $x_t = 195$, $y_t = 225$ and $\mathrm{Ca} = 0.001$ is considered.

Figure 3 provides a plot of CPU time dependence as a function of the mesh density (for four different numbers of processors) and one of speed-up dependence on the number of processors (for two problems of different size) taking flow over a square trench, $l_t = w_t = 2$ and $\mathrm{Re} = 10$ as a benchmark; the computations were performed on the advanced research computing parallel computer (ARC1) at the University of Leeds, with distributed memory architecture and fast switching. This machine has multiple hardware configurations; the one used in the present work utilised multiple nodes, each with 8 cores and 12Gb of in-core memory (1.5Gb/core). As seen from Figure 3a, the computational complexity of the algorithm is almost independent on the number of processors with the number of operations required for the calculation having almost a linear dependence on the total number of degrees of freedom: $O(\mathrm{DOF}^{1.25})$. Figure 3b, indicates that the parallel performance and scalability is relatively good in each case with better speed-ups obtained for the coarse mesh problem having DOF = 16413 (2760 elements). Nevertheless, for the finer mesh problem, with DOF = 108909 (21600 elements), even when 16 processors are used a relatively large speed-up of 12.5 is achieved. All of the results discussed subsequently were obtained using 8 processors and DOF = 794373 (172800 elements), ensuring the availability of sufficient in-core memory the calculations to be completed within a matter of hours.

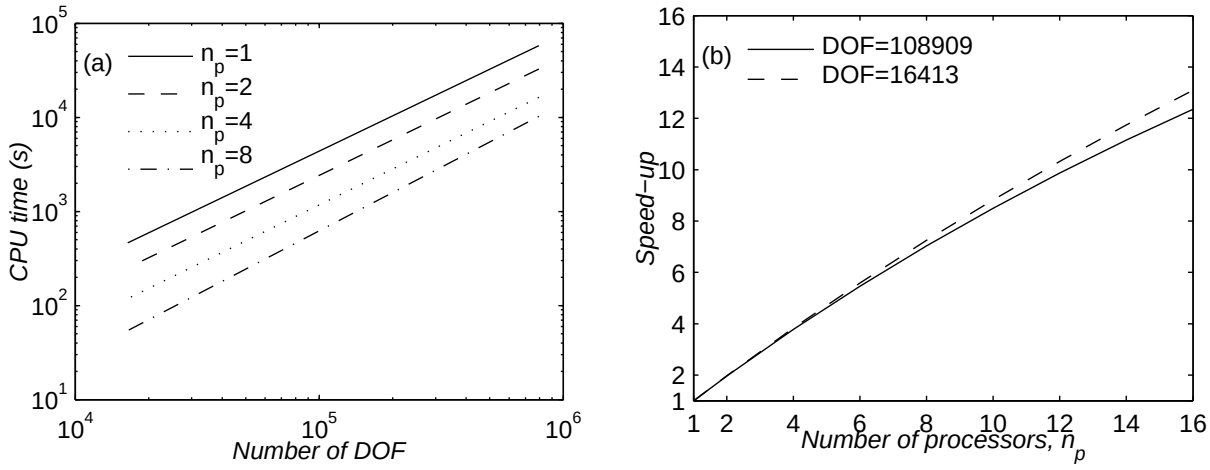

Figure 3: CPU time dependence on mesh density (left) and speed-up dependence on number of processors (right) taking flow over trench topography with $l_t = w_t = 2$, $s_0 = 1$, $\mathrm{Re} = 10$, $\mathrm{Ca} = 0.001$ and $\theta = 7^\circ$ as a benchmark.

In order to reveal the nature of the internal flow structure/topology, trajectories into and out of the flow domain are presented in Figure 4. The trajectories shown enter slightly above the trench at $z = 0.03$ and

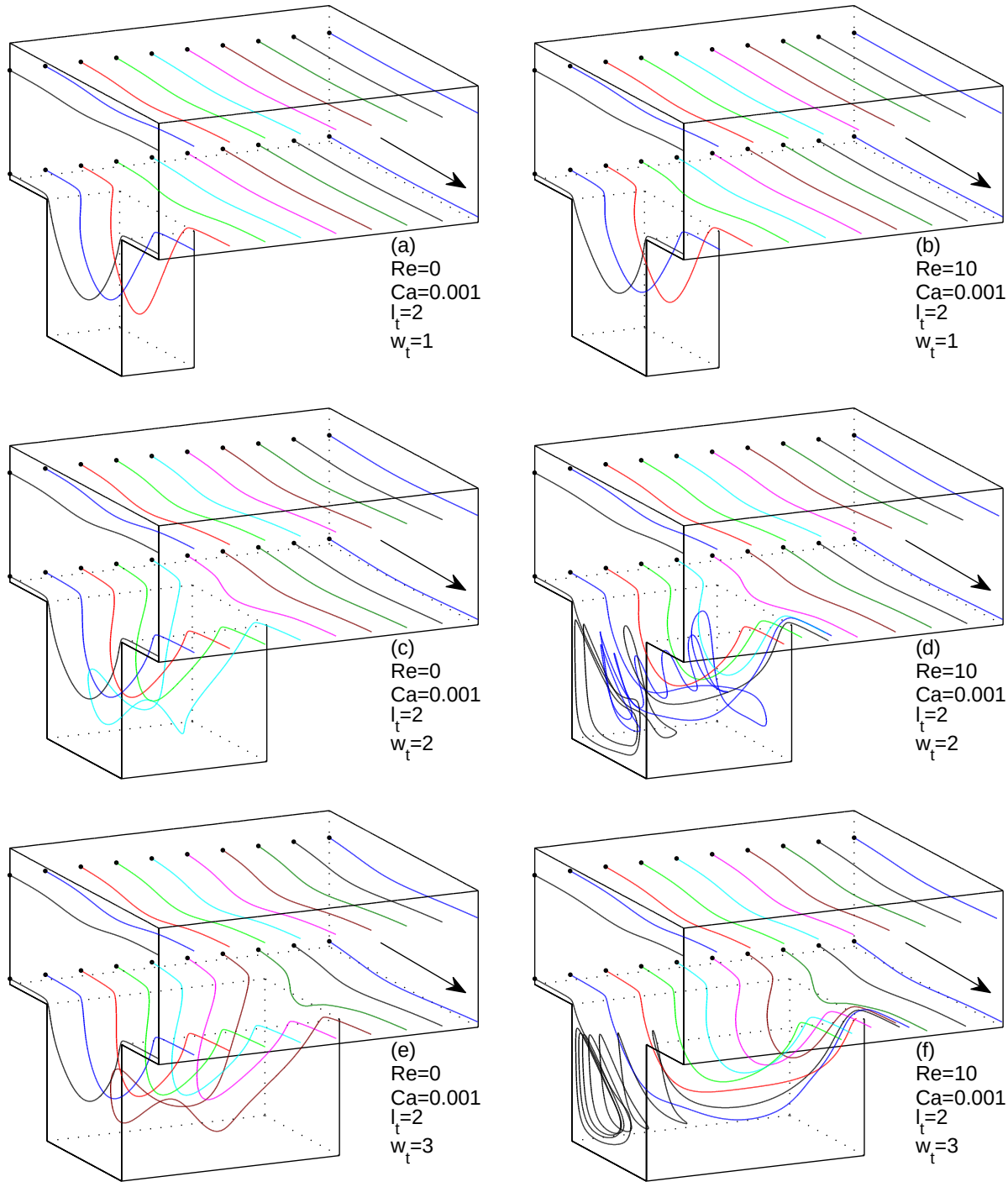

Figure 4: Three-dimensional structure of the flow, obtained by integrating along the path lines, over a localised rectangular trench topography with $l_t = 2$, $s_0 = 1$, Ca $= 0.001$ and $\theta = 7°$: $w_t = 1$ (top), $w_t = 2$ (middle) and $w_t = 3$ (bottom); Re $= 0$ (left) and Re $= 10$ (right). Starting positions are denoted as filled circles located slightly above the trench at $z = 0.04$ and close to the free surface at $z = 0.8$. For illustrative purposes different colours are used for trajectories corresponding to different starting positions. The symmetry mid-plane through the centre of the trench is on the left hand side; the closed side of the trench is on the right. The arrow shows the direction of flow.

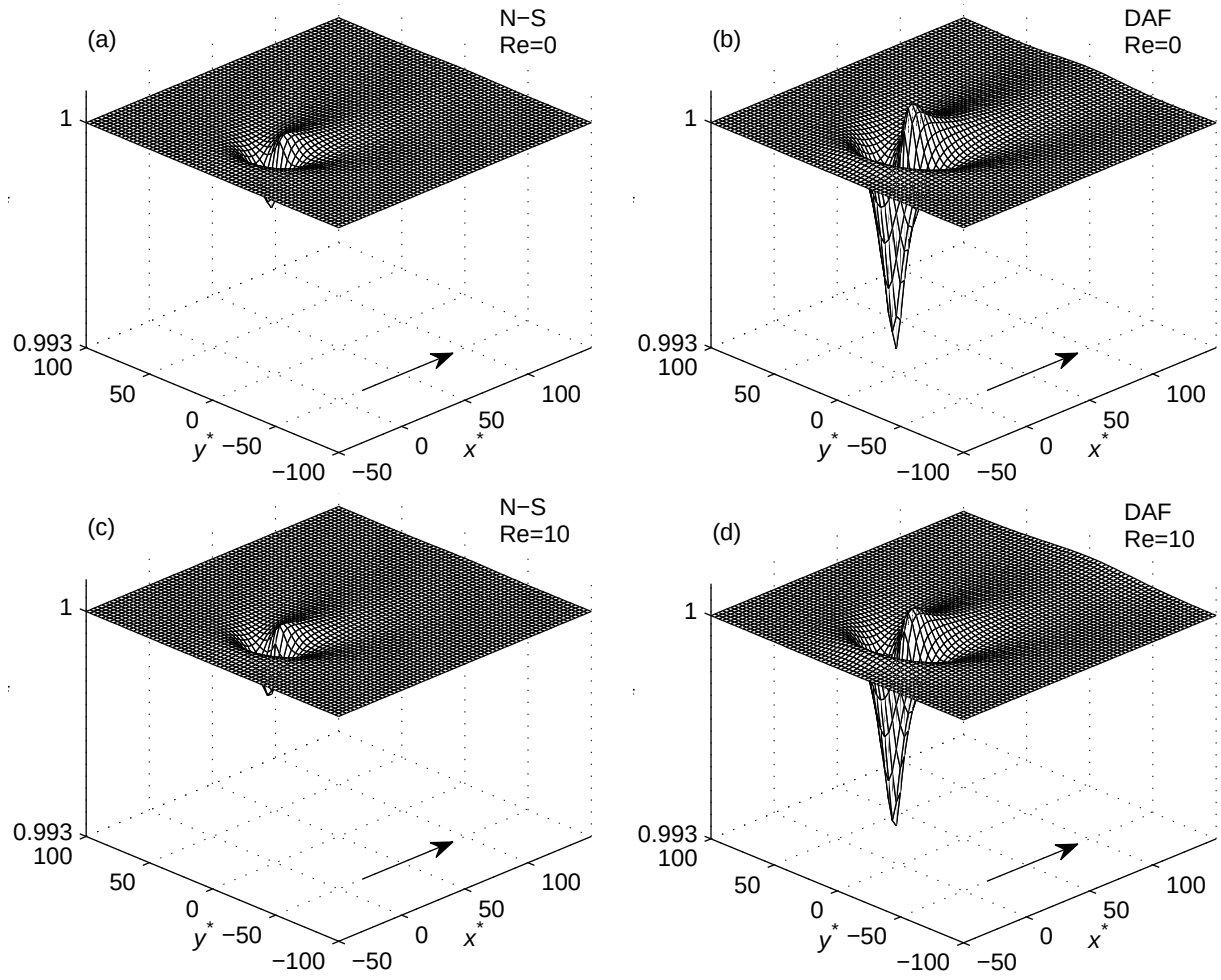

Figure 5: Comparison of predicted (N-S, left and DAF, right) three-dimensional free-surface plots for flow over a square localised trench topography with $l_t = w_t = 2$, $s_0 = 1$, Ca $= 0.001$ and $\theta = 7°$: Re $= 0$ (top) and Re $= 10$ (bottom). The arrow shows the direction of flow.

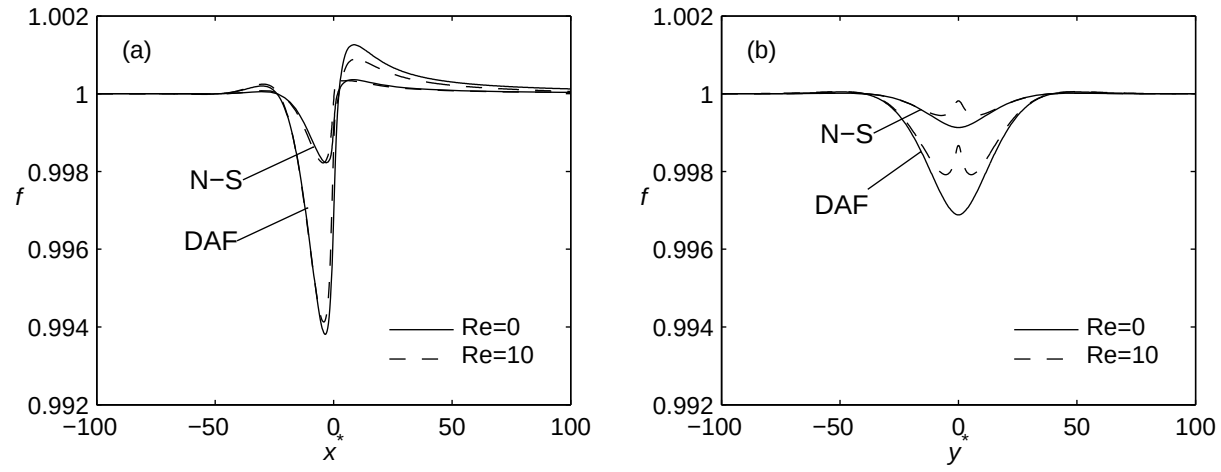

Figure 6: Predicted (N-S and DAF) streamwise (left) and spanwise (right) free-surface profiles through the centre of the localised rectangular trench topography of Figure 5, for the case Re $= 0$ and 10.

close to the free surface at $z = 0.8$, their upstream starting positions denoted as filled circles. For the sake of clarity, different colours are used to denote path-lines emanating from different starting points. It can be seen that the flow trajectories are greatly affected by the trench geometry and the presence or otherwise of inertia. For example, when Re equals both 0 and 10 and $w_t = 1$ the path-lines starting close to the left hand symmetry mid-plane (that is, the black and blue trajectories) remain close to the mid-plane. However, this is not the case when $\mathrm{Re} = 10$ and $w_t \geq 2$ in which case the trajectories after encroaching into the trench close to the mid-plane swirl around several times, during which they are laterally displaced away from the mid-plane to exit the trench close to its right hand side prior to travelling downstream. Another feature of note is observed when $\mathrm{Re} = 0$; trajectories located close to the side wall of the trench enter it only if the trench is sufficiently wide enough (see the green trajectory for $w_t = 3$ in Figure 4(e)) otherwise, $w_t \leq 2$, these trajectories (see the light-green and pink trajectories in Figure 4(a) and (c)) do not enter the trench. It can be seen also that for $\mathrm{Re} = 10$, Figure 4(b), (d), (f), the inertia present in the flow tends to straighten the path-lines making it less likely for them to enter the trench.

Having established the topological features of the flow, Figure 5 shows the free-surface disturbance experienced by the film as it passes over a square trench topography, $l_t = w_t = 2$ as in Figure 4(c) and (d); shown for comparison purposes are the corresponding free-surface disturbance predictions obtained using the model of Veremieiev et al [7] based on a long-wave approximation leading to a depth-averaged form (DAF) of the full Navier-Stokes equations, (3) to (10). Figure 6 shows the corresponding streamwise and spanwise free-surface profiles through the centre of the trench. It is clear that when the in-plane dimensions of the trench are small and comparable with the film thickness the results obtained are significantly different; the DAF solutions lead to a clear overprediction of the associated free-surface disturbances and capillary features, especially the location and magnitude of the free-surface depression. For the two methods of solution to produce comparable results the dimensions of the trench must be approximately $s_0 \ll 1 \ll l_t \approx w_t$, as for example in the case of the trench topography used in the experimental study of [20].

5 Conclusions

The flow structure and free-surface disturbance associated with the steady, stable flow of a thin liquid layer over rectangular trench topography has been explored in terms of detailed numerical solutions of the governing three-dimensional Navier-Stokes equations. The purpose written formulation involved is based on a Bubnov-Galerkin mixed-interpolation finite element scheme and parametrisation of the free-surface on the Arbitrary Lagrangian-Eulerian method of spines. The solution of the associated numerical analogue utilises a direct parallel multifrontal solver from the MUMPS library and employs a memory-efficient out-of-core approach for storing matrix cofactors on the hard drive. It is shown that the multifrontal solver provides near linear speed-up and $O(\mathrm{DOF}^{1.25})$ computational efficiency; however, at the same time is very demanding in terms of memory. The three-dimensional topology of the flow is investigated and as in the simpler case of flow over two-dimensional spanwise trench topography, [8], is shown to be dependent on both geometry and the presence of inertia. Finally, predictions from the model based on the long-wave approximation are observed to lead to significant discrepancies and unacceptable results when the in-plane dimensions of the trench topography are small and comparable to the film thickness.

References

[1] R.V. Craster and O.K. Matar. Dynamics and stability of thin liquid films. *Rev. Mod. Phys.*, 81(3):1131–1198, 2009.

[2] D.R. Walters. Disguising the leaf surface: the use of leaf coatings for plant disease control. *Eur. J. Plant Pathol.*, 114(3):255–260, 2006.

[3] D.P. Gaver and J.B. Grotberg. The dynamics of a localized surfactant on a thin-film. *J. Fluid Mech.*, 213:127–148, 1990.

[4] S.F. Kistler and P.M Schweizer, editors. *Liquid Film Coating*. Chapman and Hall, 1997.

[5] J.A. Lewis. Direct ink writing of 3d functional materials. *Adv. Funct. Mat.*, 16(17):2193–2204, 2006.

[6] N.C. Linn, C.-H. Sun, P. Jiang, and B. Jiang. Self-assembled biomimetic antireflection coatings. *Appl. Phys. Lett.*, 91(10), 2007.

[7] S. Veremieiev, H.M. Thompson, Y.C. Lee, and P.H. Gaskell. Inertial thin film flow on planar surfaces featuring topography. *Comput. Fluids*, 39(3):431–450, 2010.

[8] P.H. Gaskell, P.K. Jimack, M. Sellier, H.M. Thompson, and M.C.T. Wilson. Gravity-driven flow of continuous thin liquid films on non-porous substrates with topography. *J. Fluid Mech.*, 509:253–280, 2004.

[9] S.J. Baxter, H. Power, K.A. Cliffe, and S. Hibberd. Three-dimensional thin film flow over and around an obstacle on an inclined plane. *Phys. Fluids*, 21(3):032102, 2009.

[10] P. Hood and C. Taylor. Navier-Stokes equations using mixed interpolation. In J.T. Oden, O.C. Zienkiewicz, R.H. Gallagher, and C. Taylor, editors, *Finite Element Method in Flow Problems*, pages 121–132. UAH Press, Huntsville, 1974.

[11] S.F. Kistler and L.E. Scriven. Coating flows. In J.R.A. Pearson and S.M. Richardson, editors, *Computational Analysis of Polymer Processing*, chapter 8, pages 243–299. Elsevier Applied Science, London, 1983.

[12] I.S. Duff and J.K. Reid. The multifrontal solution of indefinite sparse symmetric linear equations. *Acm T. Math. Software*, 9(3):302–325, 1983.

[13] I.S. Duff and J.K. Reid. The multifrontal solution of unsymmetric sets of linear equations. *SIAM J. Sci. Comput.*, 5(3):633–641, 1984.

[14] P.R. Amestoy, I.S. Duff, and J.-Y. L'Excellent. Multifrontal parallel distributed symmetric and unsymmetric solvers. *Comp. Meth. Appl. Mech. Engrg.*, 184(2-4):501–520, 2000.

[15] G. Karypis, K. Schloegel, and V. Kumar. PARMETIS: Parallel graph partitioning and sparse matrix ordering library. Technical report, University of Minnesota, Minneapolis, MN, 2003.

[16] E. Agullo, A. Guermouche, and J.-Y. L'Excellent. A parallel out-of-core multifrontal method: Storage of factors on disk and analysis of models for an out-of-core active memory. *Parallel Comput.*, 34(6-8):296–317, 2008.

[17] T.B. Benjamin. Wave formation in laminar flow down an inclined plane. *J. Fluid Mech.*, 2(6):554–574, 1957.

[18] C.S. Yih. Stability of liquid flow down an inclined plane. *Phys. Fluids*, 6(3):321–334, 1963.

[19] A.E. Perry and M.S. Chong. A description of eddying motions and flow patterns using critical-point concepts. *Annu. Rev. Fluid Mech.*, 19:125–155, 1987.

[20] M.M.J. Decré and J.C. Baret. Gravity-driven flows of viscous liquids over two-dimensional topographies. *J. Fluid Mech.*, 487:147–166, 2003.